Developmental Cell
Article

A PH Domain in ACAP1 Possesses Key Features of the BAR Domain in Promoting Membrane Curvature

Xiaoyun Pang,[1,2] Jun Fan,[3] Yan Zhang,[1] Kai Zhang,[1] Bingquan Gao,[1,2] Jun Ma,[1,2] Jian Li,[4,5] Yuchen Deng,[1,2] Qiangjun Zhou,[1,8] Edward H. Egelman,[7] Victor W. Hsu,[4,5,*] and Fei Sun[1,6,*]
[1]National Laboratory of Biomacromolecules, Institute of Biophysics, Chinese Academy of Sciences, Beijing 100101, China
[2]University of Chinese Academy of Sciences, Beijing 100049, China
[3]Department of Physics and Materials Science, City University of Hong Kong, Hong Kong 999077, China
[4]Division of Rheumatology, Immunology and Allergy, Brigham and Women's Hospital, Boston, MA 02115, USA
[5]Department of Medicine, Harvard Medical School, Boston, MA 02115, USA
[6]Center for Biological Imaging, Institute of Biophysics, Chinese Academy of Sciences, Beijing 100101, China
[7]Department of Biochemistry and Molecular Genetics, University of Virginia, Charlottesville, VA 22908, USA
[8]Present address: Departments of Molecular and Cellular Physiology, Neurology and Neurological Sciences, Structural Biology, Photon Science and Howard Hughes Medical Institute, Stanford University, Stanford, CA 94305, USA
*Correspondence: vhsu@research.bwh.harvard.edu (V.W.H.), feisun@ibp.ac.cn (F.S.)
http://dx.doi.org/10.1016/j.devcel.2014.08.020

SUMMARY

The BAR (Bin-Amphiphysin-Rvs) domain undergoes dimerization to produce a curved protein structure, which superimposes onto membrane through electrostatic interactions to sense and impart membrane curvature. In some cases, a BAR domain also possesses an amphipathic helix that inserts into the membrane to induce curvature. ACAP1 (Arfgap with Coil coil, Ankyrin repeat, and PH domain protein 1) contains a BAR domain. Here, we show that this BAR domain can neither bind membrane nor impart curvature, but instead requires a neighboring PH (Pleckstrin Homology) domain to achieve these functions. Specific residues within the PH domain are responsible for both membrane binding and curvature generation. The BAR domain adjacent to the PH domain instead interacts with the BAR domains of neighboring ACAP1 proteins to enable clustering at the membrane. Thus, we have uncovered the molecular basis for an unexpected and unconventional collaboration between PH and BAR domains in membrane bending.

INTRODUCTION

Membrane remodeling is critical for many aspects of cellular function, including the biogenesis of organelles and transport carriers, cell motility, and cytokinesis. One of the best characterized protein families that participate in membrane remodeling is one that contains the BAR domain. The BAR domain can be further subclassified into four categories: F-BAR, BAR/N-BAR, I-BAR (inverse-BAR), and PinkBAR (Mim and Unger, 2012). F-BAR and BAR/N-BAR promote positive membrane curvatures through shallow or steep concave surfaces, respectively. I-BAR has a negative curvature and induces membrane extrusion. PinkBAR does not possess intrinsic curvature and acts on planar membrane surface (Pykäläinen et al., 2011).

Currently, two general mechanisms are known for how the BAR domains induce membrane curvature. One mechanism is based on scaffolding, which is initiated through dimerization that results in a banana-like structure. This structure imposes curvature on membrane through positively charged patches on the concave surface of BAR proteins that interact with the negatively charged surface of membrane through electrostatic interactions. Further cooperative membrane binding and curvature induction is achieved through tip-to-tip and lateral interactions among the dimeric BAR structures coating the membrane (Frost et al., 2008; Mizuno et al., 2010; Yu and Schulten, 2013). The other general mechanism involves membrane insertion, which typically involves an amphipathic helix, such as that seen for the N-BAR-containing endophilin (Gallop et al., 2006; Mim et al., 2012). Curiously, some BAR domains have been found to require an additional neighboring PH domain to bind membrane and induce curvature (Peter et al., 2004), but why the PH domain is required has been unclear.

ACAP1 was initially characterized as a GTPase-activating protein (GAP) for ADP-ribosylation factor 6 (ARF6) (Jackson et al., 2000). Subsequently, it was found to act also as an ARF6 effector, which involves its role as a coat component to promote endocytic recycling (Dai et al., 2004; Li et al., 2007b). ACAP1 contains four domains, with the BAR and PH domains comprising its amino portion and ArfGAP and ANK (ankryin repeat) domains comprising its carboxy portion. We recently provided a molecular explanation for how the tandem ArfGAP-ANK domains act in cargo binding by ACAP1 (Bai et al., 2012). Besides cargo binding, the other major function of coat components involves membrane bending to generate transport carriers. Here, we have sought to elucidate this role of ACAP1 through studies on its tandem BAR-PH domains.

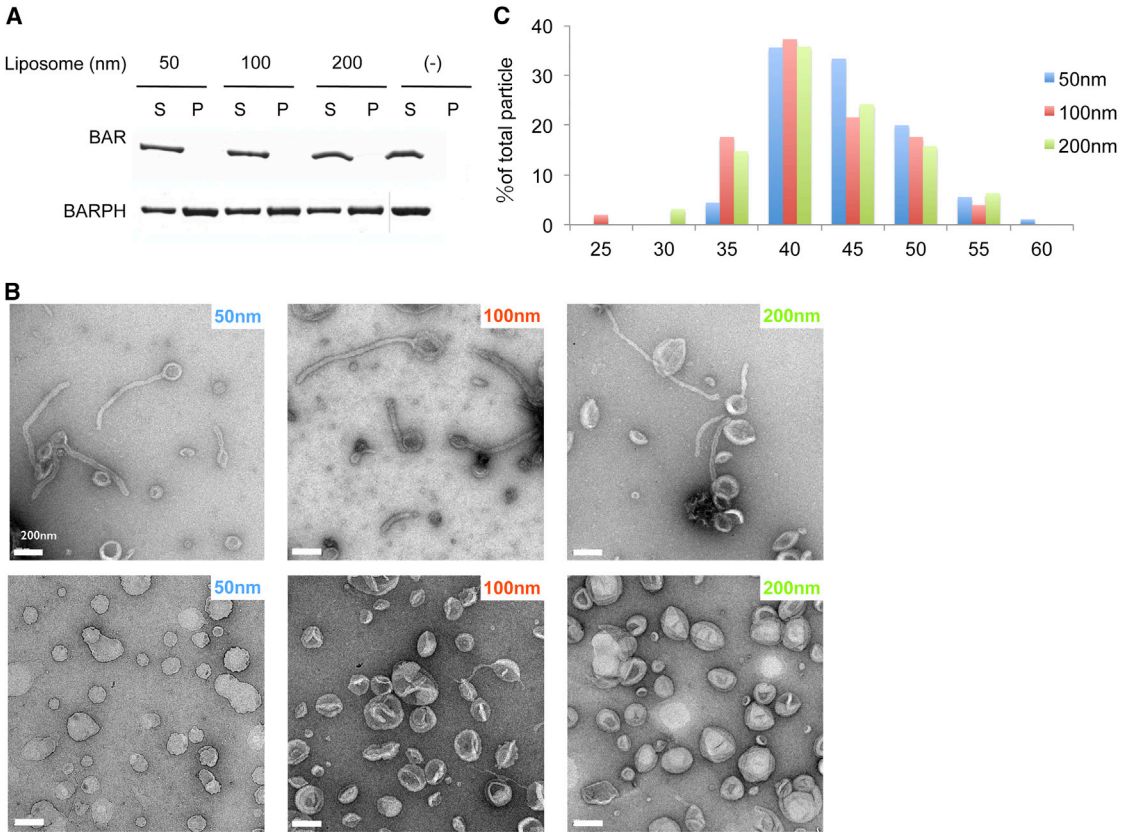

Figure 1. BAR-PH Domain of ACAP1 Is Sufficient for Membrane Binding and Tubulation

(A) Binding of different forms of ACAP1 (BAR or BAR-PH) to liposomes of varying sizes (as indicated) is assessed by centrifugation. S, supernatant; P, pellet.

(B) Negative-stain EM visualizing liposomes incubated either with (first row) or without (second row) ACAP1^{BAR-PH}; the scale bar represents 200 nm. The diameters of the liposomes are also indicated.

(C) Statistical histogram of the diameters of tubules generated by ACAP1^{BAR-PH}, plotted as a percentage of all tubules: n = 90 for 50 nm liposomes, n = 51 for 100 nm liposomes, and n = 95 for 200 nm liposomes (see also Figure S1).

RESULTS

ACAP1^{BAR-PH} Is Sufficient for Membrane Binding and Tubulation

ACAP1 has similar domain structures as multiple other members of the ArfGAP family (Figure S1A available online). Within this subfamily of ArfGAPs, ACAP2 (also known as centaurin β2) is the most similar to ACAP1. ACAP2 has been characterized previously to require its neighboring PH domain to achieve membrane binding and curvature generation (Peter et al., 2004). Thus, we focused on the corresponding tandem BAR-PH domains in ACAP1 (referred hereon as ACAP1^{BAR-PH}) for detailed analysis.

We initially generated liposomes that contained the major phospholipids of organellar membrane. To this mixture, we also added phosphatidylinositol 4,5-bisphosphate, PI(4,5)P_2, as this phosphoinositide has been found previously to promote membrane tubulation by ACAP1 (Shinozaki-Narikawa et al., 2006). The generated liposomes were then incubated with ACAP1^{BAR-PH} and analyzed for binding by centrifugation. Consistent with the previous finding on the BAR domain of ACAP2 (Peter et al., 2004), the BAR domain of ACAP1 also showed little affinity to the generated liposomes, regardless of their size (Figure 1A). In contrast, ACAP1^{BAR-PH} bound to these liposomes, which was independent of their size that ranged from 50 to 200 nm in diameter (Figure 1A).

We next found that ACAP1^{BAR-PH} also induces membrane curvature, as reflected by the tubulation of liposomes, which was visualized by negative-stain electron microscopy (EM) (Figure 1B). The diameters of membrane tubules were similar regardless of the liposome size added to the incubation, with quantitation revealing 44.7 ± 5.0 nm for liposomes of 50 nm diameter (n = 90), 42.4 ± 5.8 nm for liposomes of 100 nm diameter (n = 51), and 42.7 ± 5.8 nm for liposomes of 200 nm diameter (n = 95) (Figure 1C). Thus, different from the properties of prototypic F-BAR and N-BAR proteins, whose ability to induce membrane tubulation is dependent on liposome size (Shimada et al., 2007), ACAP1^{BAR-PH} can act on a range of liposome sizes to induce membrane tubules that have relatively constant diameters.

Crystal Structure of ACAP1^{BAR-PH}

To understand how ACAP1^{BAR-PH} imparts membrane curvature, we next solved its crystal structure to 2.2 Å resolution by the single wavelength anomalous diffraction method (Table 1). As

Table 1. Crystallographic Data Collection and Refinement Statistics for ACAP1^{BAR-PH}

	ACAP1^{BAR-PH}	Se-ACAP1^{BAR-PH}
Data Collection and Processing		
Space group	$P2_1$	$P2_1$
Cell Dimensions		
a, b, c (Å)	42.5, 59.7,168.9	42.4, 59.8, 169.2
α, β, γ (°)	90.0, 91.4, 90.0	90.0, 91.1, 90.0
Wavelength (Å)	1.0000	0.9790
Resolution (Å)	50.0–2.20 (2.24–2.20)	50.0–2.90 (2.95–2.90)
R_{merge} (%)	8.2 (41.8)	12.3 (55.2)
$<I/\sigma(I)>$	21.3 (3.9)	14.7 (1.34)
Completeness (%)	96.9 (95.6)	98.4 (81.9)
Redundancy	3.6 (3.2)	6.9 (4.4)
Refinement		
Resolution (Å)	30.0–2.20	
No. reflections	41,114	
R_{work}/R_{free}	0.211/0.266	
Number of Atoms		
Protein	5,839	
Water	146	
B Factors(Å^2)		
Protein	24.22	
Water	23.22	
Rmsds		
Bond lengths (Å)	0.013	
Bond angle (°)	1.458	

Corresponding parameters for the highest resolution shell are shown in parentheses.

would be predicted for a BAR-containing protein, the structure appears as a banana-shaped dimer within one asymmetric unit (Figure 2A). The final refined model contains 364 residues (aa 1–364) for one monomer and 361 residues (aa 1–361) for the other. The BAR domains within the dimer form a bundle that contains eight helices, which is similar to the BAR domains of APPL1 and APPL2 (King et al., 2012; Li et al., 2007a; Zhu et al., 2007), but different from other reported BAR domains (Gallop et al., 2006; Peter et al., 2004; Pykäläinen et al., 2011; Shimada et al., 2007). The dimer interface has a large area (5,900 Å^2) and contains mainly hydrophobic residues that likely mediate dimerization. Dimerization of ACAP1^{BAR-PH} was confirmed from size exclusion chromatography and light scattering (Figure S2A). The in vitro disassociation constant of the dimerization was calculated to be below 5 μM, according to the quantitative gel-filtration experiment (Figure S2B), which is lower than the reported constant for the N-BAR protein endophilin A2 (Ross et al., 2011). This higher affinity could be attributed to the larger dimerization interface (5,900 Å^2) of ACAP1^{BAR-PH}.

The BAR domain in each monomer contains five helices: α0, α1, α2, α3, and α4 (Figures 2A and S1B). Helix α1, α2, and α3 form an antiparallel coiled-coil, and helix α4 forms a helical bundle with the antiparallel coiled-coil of another monomer. This is followed by the PH domain (Figures 2A and 2B), which contains a seven-stranded β barrel (β1–β7) followed a helix (α5) that is located at the extreme carboxy terminus (Figures 2B and S1B).

The two PH domains are positioned at the opposite ends of the dimeric structure. Moreover, the relative positions between the PH and BAR domains are not identical when the two monomers are superimposed by aligning the BAR domains (Figure S2C). A linker region (from residue 249 to 267) between the BAR and PH domains (Figure S1B) suggests the possibility of flexibility in the movement of the PH domain. Indeed, this feature turned out to be important for membrane binding and bending by ACAP1^{BAR-PH} (to be detailed further below).

In comparison to other BAR structures, such as those from APPL1 (Li et al., 2007a; Zhu et al., 2007), the N-BAR Amphiphysin (Peter et al., 2004), and the F-BAR FBP17 (Shimada et al., 2007) (see also Figure S2D), the positive curvature of ACAP1^{BAR-PH}, which is ~1/40nm^{-1} (Figure 2A), is smaller than that of APPL1 (~1/17 nm^{-1}) and amphiphysin (~1/22 nm^{-1}), but larger than that of FBP17 (~1/60 nm^{-1}). Although the overall fold of ACAP1^{BAR-PH} is similar to that of the tandem BAR-PH domains in APPL1 (Li et al., 2007a; Zhu et al., 2007), the structural rmsd (root mean square deviation) of the BAR domains between ACAP1 and APPL1 is 2.9 Å for 190 aligned Cα atoms. Furthermore, there is an ~20° outward rotation of helix α4 in ACAP1^{BAR-PH} when compared with that of APPL1 (Figure S2E). This feature explains the more shallow curvature formed by ACAP1^{BAR-PH} as compared with the corresponding counterpart in APPL1.

Studies on multiple PH domains have revealed a common β1/β2 loop that plays a key role in binding to phosphoinositides (Ceccarelli et al., 2007; Cronin et al., 2004; Ferguson et al., 2000). However, when compared with these PH domains, such as that of DAPP1 and Grp1 (Figure S2F), the corresponding region in the PH domain of ACAP1 (site 1; Figures 2B and 2C) exhibits less positive electrostatic potential and also forms a less significant cavity for binding to an inositol group. The PH domain of ArhGAP9 has been shown previously to bind inositol trisphosphate at an opposite site to the β1/β2 loop (Ceccarelli et al., 2007) (see also Figure S2G). The corresponding site in ACAP1 (site 2; Figures 2B and 2C) shows similar electrostatic potential but different surface contour. Collectively, these structural comparisons suggest that the PH domain of ACAP1 may form binding pockets that would have less specificity toward a particular phosphoinositides species. Indeed, revisiting the liposome binding assay, we found that ACAP1^{BAR-PH} can bind to a range of phosphoinositides, including PI(3)P, PI(4)P, PI(5)P, PI(3,4)P_2, PI(3,5)P_2, PI(4,5)P_2, and PI(3,4,5)P_3 (Figure 2D). We also found that ACAP1^{BAR-PH} cannot bind liposomes that contain PI (Figure 2D), suggesting that the binding pocket in the PH domain only recognizes inositol ligands when they are phosphorylated. These binding results were also quantified (Figure 2E).

A Positively Charged Patch in the PH Domain Contributes Importantly to Membrane Binding

Previous elucidations have revealed that the banana-like structure formed through the dimerization of the BAR domain binds to the negatively charged membrane surface through positively charged patches on the concave surface of the BAR structure (Itoh and De Camilli, 2006; Peter et al., 2004; Shimada et al., 2007). On the concave surface of the BAR domain in ACAP1, we also noted multiple positively charged patches, specifically

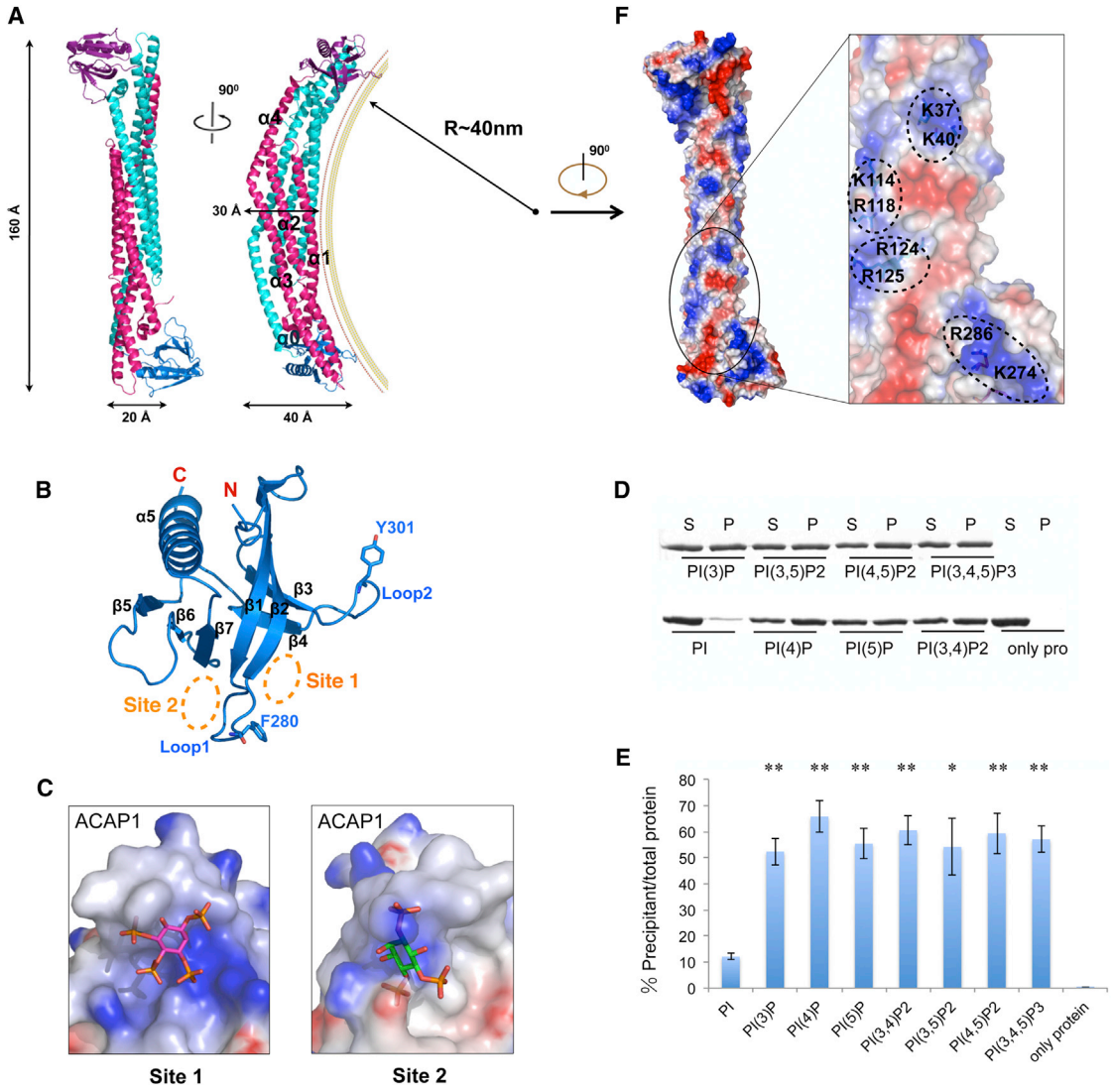

Figure 2. Crystal Structure ofACAP1^{BAR-PH}

(A) Overall structure of dimeric ACAP1^{BAR-PH}. The two BAR domains are shown in cyan and pink, while the corresponding PH domains are colored in magenta and blue, respectively. Secondary structural elements of BAR domain are labeled as indicated. A hypothetic membrane is depicted according to the curvature (40 nm^{-1}) of the BAR domains.

(B) Structure of PH domain in cartoon representation. Secondary structural elements are labeled as indicated. Relevant residues (F280 and Y301) in Loop1 and Loop2 are shown as stick structures. The potential phosphoinositides binding sites (site 1 and site 2) are indicated via the orange dashed circles.

(C) Site 1 and site 2 in the PH domain of ACAP1. The electrostatic potential is mapped onto the surface of the structures, with blue coloring positive charge and red coloring negative charge. The docked inositol ligands for the binding pockets are shown as stick models. For site 1, the docked Ins(1,3,4,5)P_4 is based on the crystal structure of DAPP1 (PDB code, 1FAO). For site 2, the docked Ins(1,4,5)P_3 is based on the crystal structure of ArhGAP9 (PDB code, 2P0D).

(D) The binding of ACAP1^{BAR-PH} to liposome that contains various phospholipids (as indicated) is assessed by centrifugation. S, supernatant; P, pellet.

(E) Quantitation of results in (D). The level of pelleted protein is expressed as the percentage of the total protein input. All error bars represent SD from three independent experiments. The significances of the differences in comparison to PI containing liposome are expressed as $^{**}p < 0.001$ and $^{*}p < 0.01$.

(F) Electrostatic surface representation on the concave surface of ACAP1^{BAR-PH} and a closeup view of the positively charged patches, with blue coloring positive charges and red coloring negative charges (see also Figure S2).

K37/K40, K114/R118, and R124/R125 (Figures 2F and S1B). Thus, we targeted these residues for mutagenesis, which involves substitutions with alanines, and also by substituting lysines with aspartates and arginines with glutamates. These mutations resulted in mild to modest decreases in liposome binding by ACAP1^{BAR-PH}, as confirmed by quantitation (Figure 3A), suggesting that the positively charged patches in the BAR domain do not constitute the main determinant for membrane binding by ACAP1^{BAR-PH}.

We next considered that the concave surface of the banana-like structure of ACAP1^{BAR-PH} extends to the PH domain (Figure 2A). Intriguingly, there exists a positively charged patch on this side of the PH domain, K274/R286 (Figure 2F). When this patch was mutated, again by substituting with alanines, or by

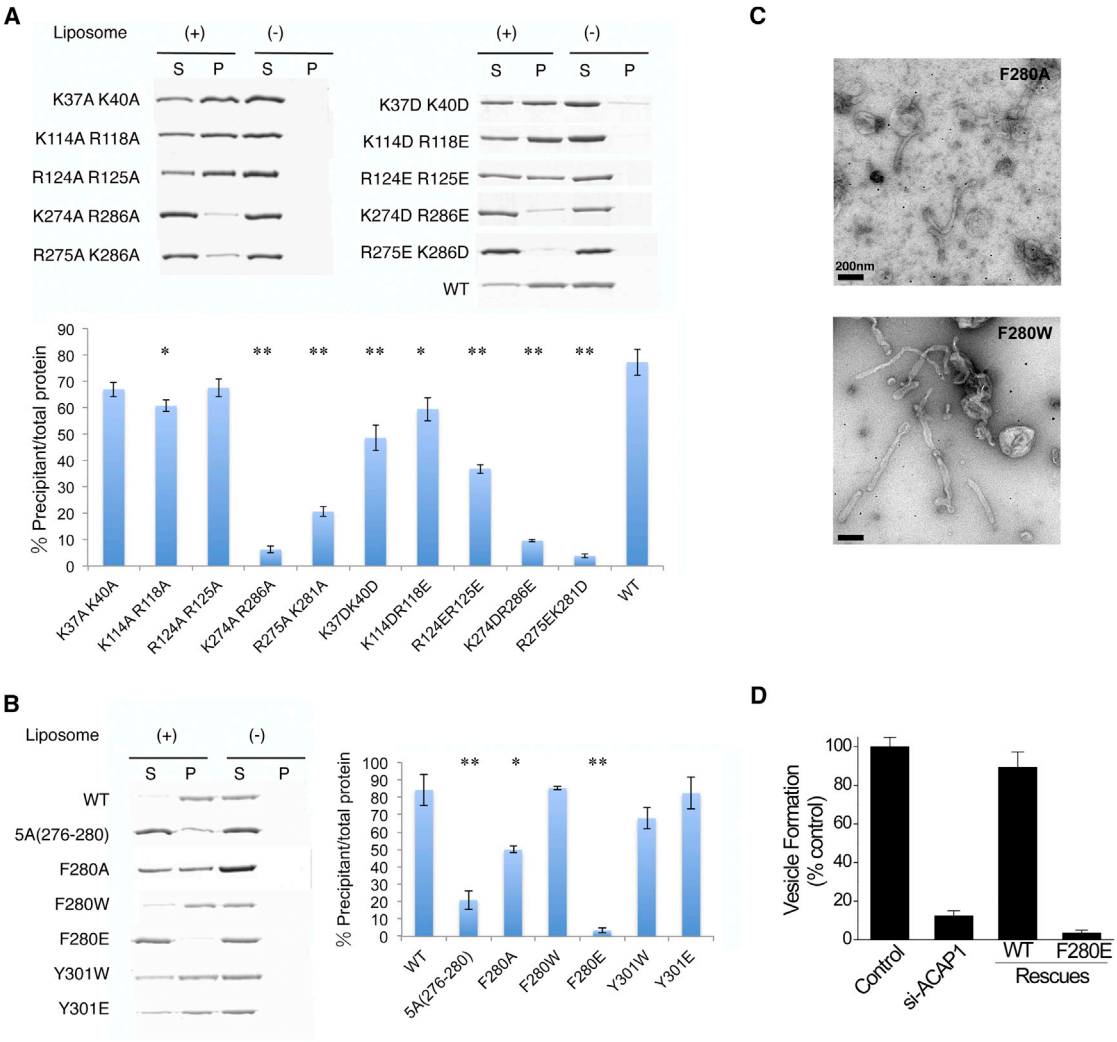

Figure 3. Mutagenesis Studies to Assess Membrane Binding and Tubulation

(A) Binding of mutant forms of ACAP1$^{BAR\text{-}PH}$ (as indicated) to liposomes is assessed by centrifugation. S, supernatant; P, pellet. The top panel shows a representative result, while the bottom panel shows quantitation from three independent experiments. All error bars represent the SD from three independent experiments. The degree of significance involves comparison between wild-type and different mutants, with $^{**}p < 0.001$ and $^{*}p < 0.01$.

(B) Binding of mutant forms of ACAP1$^{BAR\text{-}PH}$ (as indicated) to liposomes is assessed by centrifugation. S, supernatant; P, pellet. The left panel shows a representative result, while the right panel shows quantitation from three independent experiments. All error bars represent the SD from three independent experiments. The degree of significance involves comparison between wild-type and different mutants, with $^{**}p < 0.001$ and $^{*}p < 0.01$.

(C) Negative-stain EM visualizing liposome tubulation induced by two mutant forms of ACAP1$^{BAR\text{-}PH}$ (as indicated); the scale bar represents 200 nm.

(D) The reconstitution of recycling vesicles from endosomal membrane was performed by incubating membrane and cytosol fractions derived from HeLa cells and then tracking the redistribution of a recycling cargo, TfR, from the compartmental membrane fraction to the vesicular membrane fraction. Cytosol was derived from cells with different treatment as indicated. The level of vesicle formation after the incubation was then quantified (see also Figure S3). All error bars represent the SD from three independent experiments

substituting lysines with aspartates and arginines with glutamates, we detected a more dramatic effect on liposome binding by ACAP1$^{BAR\text{-}PH}$ (Figure 3A). Thus, unlike the conventional BAR domains, the BAR domain in ACAP1 requires cooperation from the PH domain for membrane binding.

A Loop in the PH Domain Contributes Importantly to Both Membrane Binding and Curvature Induction

We then noted another intriguing feature of the PH domain in ACAP1. Near the vicinity of the positively charged patch characterized above is a predicted loop. This structure, Loop1 (aa 276–282, ASNAFKT), occurs between the β1 and β2 folds of the PH domain (Figure 2B), which could potentially insert into the membrane, when the overall orientation of the ACAP1$^{BAR\text{-}PH}$ structure is considered with respect to the membrane (Figure 2A). In addition, by aligning the structures of PH domains between ACAP1 and Grp1, a corresponding loop is predicted to exist in Grp1, which has also been suggested previously to penetrate into lipid bilayer (Lumb et al., 2011) (see also Figure S2H). Thus, to test whether Loop1 can be involved in membrane insertion, we

mutated the residues (276–280) in Loop1 to alanines. We found that the resulting mutant form of ACAP1^{BAR-PH}, 5A (276–280), exhibits substantially decreased binding to the membrane (Figure 3B).

We next noted that an aromatic residue (F280) resides near the distal region of Loop1, which could potentially be important for membrane insertion. Focusing on this residue, we first mutated it to alanine, which weakened the membrane binding by ACAP1^{BAR-PH} (Figure 3B). When F280 was mutated more dramatically to glutamate, we found that membrane binding by ACAP1^{BAR-PH} was virtually eliminated (Figure 3B). Consistent with the bulky hydrophobic nature of F280 being important, we found that a more conservative mutation of F280 to tryptophan (F280W) allows membrane binding by ACAP1^{BAR-PH} to be preserved (Figure 3B).

We next examined mutations in the F280 residue with respect to the ability of ACAP1^{BAR-PH} to induce membrane curvature. Point mutant forms were incubated with liposomes and then examined by EM. We found that F280 is also critical for the induction of membrane curvature (Figure 3C). In particular, mutation of this residue to alanine (F280A) reduced the ability of ACAP1^{BAR-PH} to induce liposome tubulation, while a more conservative mutation (F280W) preserved the ability to tubulate liposomes.

We also sought confirmation that a critical role for the F280 residue in membrane insertion underlies the ability of ACAP1 to act as a coat component in generating recycling vesicles from endosomal membrane. We had previously established a reconstitution system to show that ACAP1 acts in vesicle formation from endosomal membrane, which involved the incubation of membrane and cytosolic fractions and then tracking the redistribution of a recycling cargo from compartmental membrane to vesicular membrane (Li et al., 2012). Taking a similar approach, which in this case involves the incubation of membrane and cytosolic fractions derived from HeLa cells and then tracking the redistribution of the recycling transferrin receptor (TfR) between these two fractions, we found that, whereas cytosol that expressed the wild-type ACAP1 promotes vesicle formation, cytosol that expressed the mutant ACAP1 (F280E) shows markedly impaired ability (Figure 3D). Thus, the result confirmed that the F280 residue in ACAP1 is also critical for its ability to act as a coat component in promoting vesicle formation.

We also noted that, besides Loop1, the PH domain is predicted to possess another loop structure, Loop2 (aa 299–305), which resides between β3 and β4 (Figure 2B). Although this loop also contains a bulky hydrophobic residue (Y301), it is predicted to be oriented less favorably with respect to the possibility of inserting into the membrane. As confirmation, we mutated Y301 in Loop2 to either tryptophan (Y301W) or glutamate (Y301E) and found that either mutation has minimal effects on membrane binding by ACAP1^{BAR-PH} (Figure 3B). Thus, the result suggested that Loop2 is less likely to be involved in membrane insertion by ACAP1.

N-Terminal Helix α0 of ACAP1^{BAR-PH} Is Not Involved in Membrane Interaction

In some BAR domains, an N-terminal amphipathic helix, such as that seen in endophilin, has been elucidated to be important for membrane insertion and curvature induction (Bai et al., 2010; Boucrot et al., 2012; Gallop et al., 2006). The N-terminal short helix α0 (residues 6-12, DFEECLK) of ACAP1^{BAR-PH} exhibits a semiamphipathic pattern according to helical wheel analysis (http://rzlab.ucr.edu/scripts/wheel/wheel.cgi), having hydrophobic surface on one side and charged surface on the other (Figure S3A). However, the crystal structure of the dimer suggested that helix α0 forms close contacts with helices α1, α2, and α3 of the same monomer and also additional contacts with the other monomer, via both hydrophobic and electrostatic interactions (Figure S3A). These interactions suggested that helix α0 might not be sufficiently flexible to participate in membrane insertion. As a confirmation, we deleted the first 12 residues of ACAP1^{BAR-PH} and found that they had no significant effect on membrane binding (Figure S3B) or membrane tubulation (Figure S3C) of liposomes. Thus, the N-terminal helix α0 is unlikely to act in membrane insertion.

Cryoelectron Microscopy of Liposomes Coated with ACAP1^{BAR-PH}

Having defined the key features of the PH domain that enable the ACAP1^{BAR-PH} structure to bind and bend membrane, we next sought further insight into how it achieves this role by pursuing cryoelectron microscopy (cryo-EM). After incubation of ACAP1^{BAR-PH} with liposome, the sample was flash frozen and subjected to cryo-EM observation. From the cryo-EM micrographs, we observed that some liposomes are multilamellar and that only the outer layer can be detected to have coating by the ACAP1^{BAR-PH} protein while the inner layer appears as smooth uncoated membrane (Figure 4A). This observation suggested that the coating observed on liposomal membrane is unlikely due to artifacts, such as cryo-EM imaging noise or defocusing effects. Pursuing cryoelectron tomography, we measured the thickness of the coated layer to be about 8 nm (Figure 4B; Movie S1), which is thicker than the width (~4 nm) but not the length (~16 nm) of the banana-like structure formed by the dimerization of ACAP1^{BAR-PH} (Figure 2A), suggesting that ACAP1^{BAR-PH} binds to the liposome membrane in a tilted orientation.

We then focused on the tubulated portions of liposomes coated by ACAP1^{BAR-PH} (Figure 4C). The diameters of these tubules were in the range of 40 to 50 nm (Figure S4A), which is similar to our previous measurement of these tubules based on negative-stain EM (Figure 1C). Portions of the tubules were selected to generate a density profile across the diameter of the tubule (Figure 4D). The membrane bilayer could be easily discerned, and the thickness of the protein coat was measured to be about 6 nm (Figure 4D). The thickness of this coating varied depending on whether the measurement was taken on the tubulated or the nontubulated portion of the liposome, suggesting a different assembly of ACAP1^{BAR-PH} on the membrane on tubulation.

We next performed 3D reconstructions of the linear portions of the tubules (boxed region in Figure 4D), which were segmented for image analysis and classification. The spiral feature of some class averages (Figure 4E) suggested helical symmetry in the packing of ACAP1^{BAR-PH} on the tubules, which was further confirmed based on the layer-line diffraction patterns of selected well-ordered long tubules (Figure 4F). Two types of helical diffraction patterns were observed and indexed, class I and II (Figure 4F). We utilized an iterative helical real space

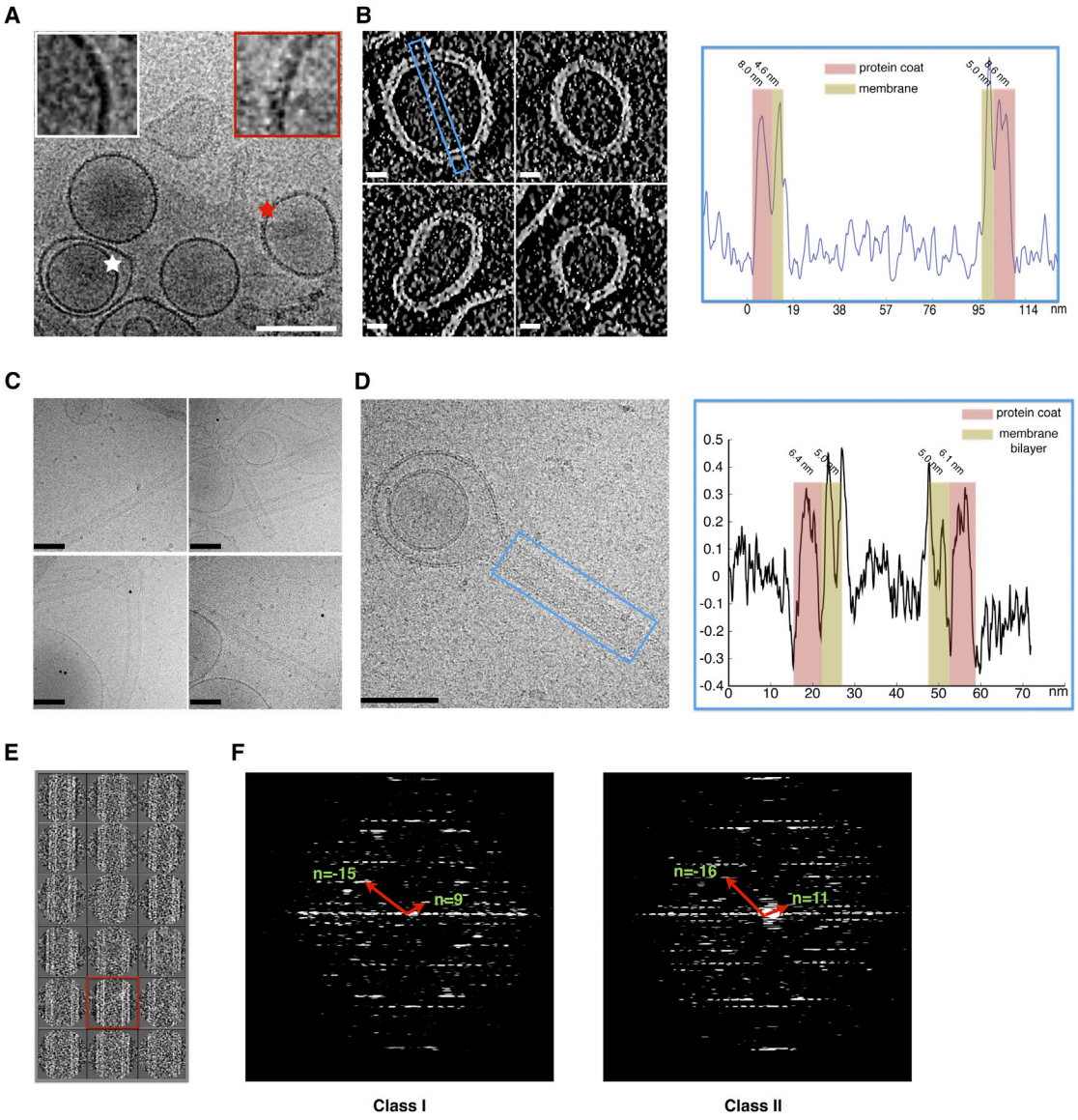

Figure 4. Cryo-EM of ACAP1^{BAR-PH} Coating Liposomal Membrane

(A) Raw cryo-EM micrograph of ACAP1^{BAR-PH} coating liposomes. The coated outer lamellar and the uncoated inner lamellar are indicated by red and white stars, respectively; bar, 100 nm. The insets show magnified views.

(B) Cryo-EM tomograms of liposomes coated with ACAP1^{BAR-PH}; the scale bar represents 20 nm (left panel). A region was selected for line-scanning analysis, as highlighted by the blue rectangle. The integrated density across the liposome is plotted, with the regions for protein coat and membrane indicated and thickness labeled (right panel).

(C) Raw cryo-EM micrographs of tubules coated with ACAP1^{BAR-PH}; the scale bar represents 100 nm.

(D) Cryo-EM micrograph of liposome with tubule coated with ACAP1^{BAR-PH} ; the scale bar represents 100 nm (left panel). A region was selected for line-scanning analysis, as highlighted by the blue rectangle. The integrated density across the tubule is plotted, with the regions for protein coat and membrane indicated and thickness labeled (right panel).

(E) 2D classification of images showing dynamics of ACAP1^{BAR-PH} coating liposomal tubules.

(F) Helical diffraction patterns of tubules exemplifying class I and class II. The Bessel functions for basis vectors are shown and labeled accordingly (see also Movie S1).

reconstruction (IHRSR) approach (Egelman, 2000) to determine the 3D structures of these two classes. The layer-line diffraction patterns of the final reconstructed cryo-EM maps (Figure S4B) matched the ones of the original micrographs (Figure 4F), and further validations of the reconstructions were provided via the match of maps with the atomic models (below). We achieved ~14 Å resolution for class I and ~17 Å resolution for class II, as assessed by a visual comparison between the cryo-EM maps and the fitted crystallography structural models. These two resolutions are between the ones based on the 0.5- and 0.143-cutoff criterions on the Fourier shell correlation (FSC) curves (Figures S4C and S4D).

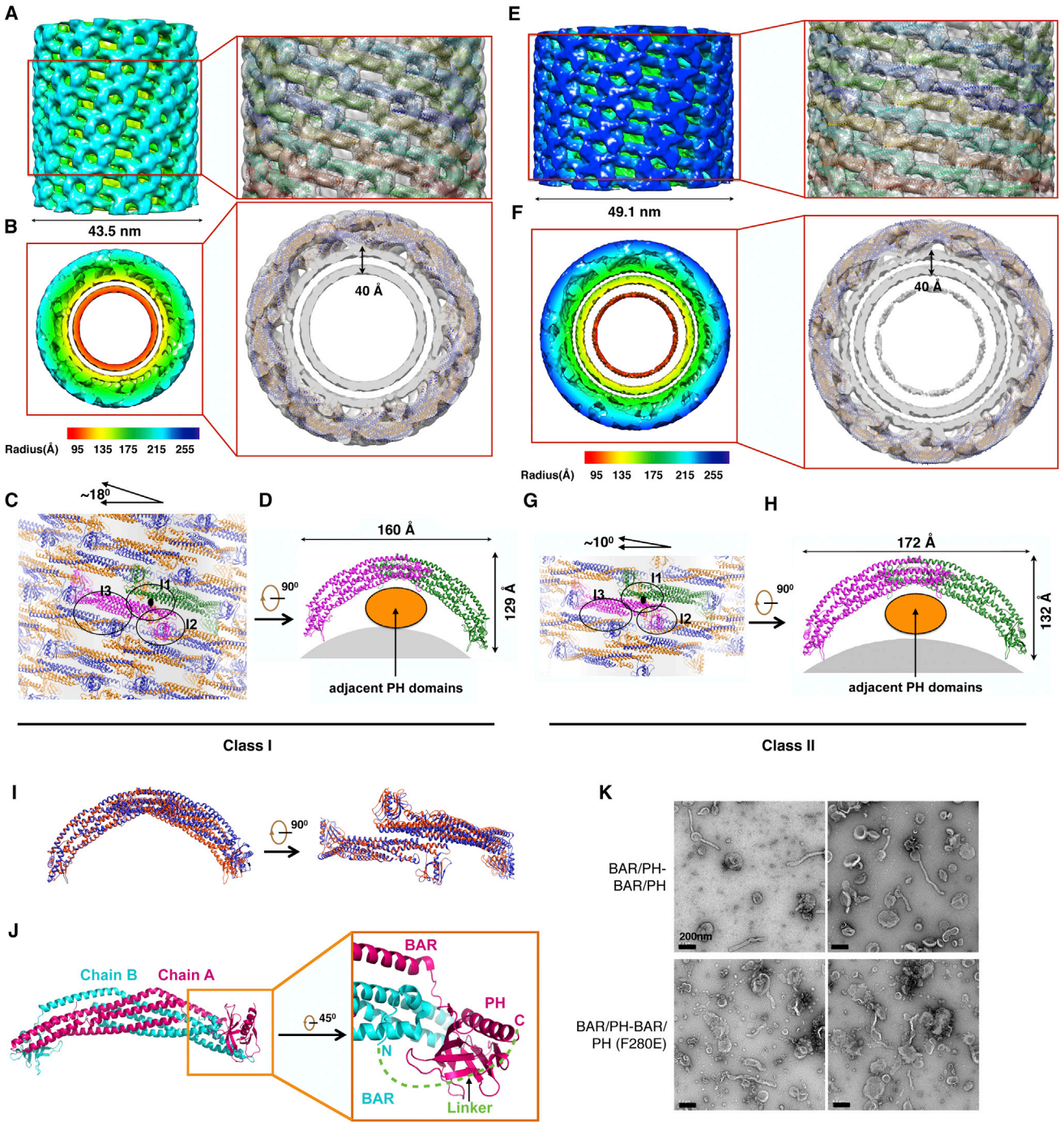

Figure 5. 3D Reconstructions of ACAP1^{BAR-PH} Coating Tubules

(A and B) Cryo-EM map of a liposomal tubule coated with ACAP1^{BAR-PH} in class I that is shown in isosurface representation with the side view in (A) and top view in (B). The map is colored according to the cylinder radius from red to blue. The structural models of ACAP1^{BAR-PH} in cartoon representation are fitted into the map and shown on the right. In (B), the two chains of ACAP1^{BAR-PH} dimer are colored in gold and blue, respectively, and the thickness of the double-layer membrane is labeled.

(C and D) Structural model of ACAP1^{BAR-PH} helical assembly on the class I liposomal tubule. The ACAP1^{BAR-PH} tetramer in one asymmetric unit, colored in magenta for one dimer and green for another, is shown with the top view in (C) and side view in (D). The interaction interfaces (I1, I2, and I3) for ACAP1^{BAR-PH} helical assembly are indicated by black circles and labeled in (C). The titling angle of ACAP1^{BAR-PH} tetramer with respect to the cross section of the tubule is depicted on the top. In (D), the membrane region is shown in gray.

(E and F) Cryo-EM map of a liposomal tubule coated with ACAP1^{BAR-PH} in class II that is shown in the side view (E) and the top view (F). The structural models of ACAP1^{BAR-PH} in cartoon representation are fitted into the map and shown on the right. The color and labeling schemes are the same as that described in (A) and (B).

(legend continued on next page)

The cryo-EM map revealed the class I tubule to have a diameter of 43.5 nm, with the double membrane thickness of 4.0 nm and the ACAP1^{BAR-PH} coating thickness of 6.0 nm (Figures 5A and 5B). We then sought to fit the structural model of ACAP1^{BAR-PH} into the cryo-EM map in determining how the ACAP1^{BAR-PH} molecules could assemble on the tubulated liposome (Figures 5A and 5B; Movies S2 and S3). The analysis suggested that two ACAP1^{BAR-PH} molecules pack laterally with each other via the interactions between BAR domains and thereby assemble into an ACAP1^{BAR-PH} tetramer with a 2-fold symmetry (Figures 5C and 5D). The resulting tetramer exhibited an elongated banana-like shape with two PH domains interacting with the membrane and two other PH domains not interacting with the membrane. The tetramer formed an asymmetric unit of the ACAP1^{BAR-PH} helical packing on the tubule, and the tilting angle with respect to the tubular cross-section was ~18°. In this configuration, the tetramers were observed to pack onto the membrane via lateral interactions and "end-to-arch" interactions in which one tetramer inserts its end underneath the adjacent tetramer arch. Consequently, the convex part of the cryo-EM map is composed of the arches and ends of tetramers, while the concave part is composed of lateral interacting BAR domains (Figure 5A). From the cross-section of the cryo-EM map (Figure 5B), the connection densities between the protein layer and the membrane could be clearly observed, which fitted well with Loop1 of the PH domain interacting with the membrane. Furthermore, only one monomer of the ACAP1^{BAR-PH} dimer was observed to insert its Loop1 into the membrane.

Inspection of the ACAP1^{BAR-PH} helical packing suggested three main interfaces (Figure 5C). One interface (labeled I1 in Figure 5C) would occur through the formation of tetramers of ACAP1^{BAR-PH}, which involves their BAR domains. A second interface (labeled I2 in Figure 5C) occurs through "end-to-arch" interactions between tetramers, which are achieved by a PH domain that does not contact the underlying membrane interacting with an adjacent BAR domain. A third interface (labeled I3 in Figure 5C) occurs through lateral interactions among tetramers. Moreover, based on the residues likely to be involved in these interactions, they are predicted to be mainly electrostatic.

In contrast to class I tubules, class II tubules exhibit different helical symmetries (Figure 4F) and a longer diameter of 49.1 nm (Figure 5E). Nevertheless, the cryo-EM reconstruction of class II tubules suggested a similar helical packing of ACAP1^{BAR-PH} on membrane (Figures 5E–5H; Movies S4 and S5). The asymmetric unit of class II tubules was still the tetramer of ACAP1^{BAR-PH}, although with a smaller tilting angle of ~10°. Moreover, the tetramer assembly occurs via similar lateral and "end-to-arch" interactions (Figure 5G). The extended length of the banana-like tetramer in class II tube was 172 Å, while the extended length was 160 Å for class I tubules (Figures 5D, 5H, and 5I). No other significant differences were observed between the tetramers in classes I and II (Figure 5I).

Overall, by inspecting the cryo-EM reconstructions of the tubulated liposomes coated with ACAP1^{BAR-PH}, we uncovered multiple remarkable findings. First, the interaction between the coating protein and the membrane is mediated by one PH domain of the ACAP1^{BAR-PH} dimer. Second, there is no significant interaction between the BAR domain and the underlying membrane. Instead, the BAR domain contributes to the packing interfaces among ACAP1^{BAR-PH} protein in assembling the coating on liposome membrane. Third, the PH domain in the ACAP1^{BAR-PH} dimer that does not contact the membrane interacts with the BAR domain of the adjacent dimer. As such, these collective findings reveal a distinctly different mechanism by which the BAR-containing ACAP1 achieves tubule formation, as compared with those previously elucidated for a prototypic F-BAR protein (Frost et al., 2008) and an N-BAR protein (Mim et al., 2012). Whereas those BAR-containing proteins achieve membrane binding and bending through the BAR domain playing the principal role, which involves either electrostatic interactions with membrane or insertion of a hydrophobic structure into membrane, we have found that the neighboring PH domain possesses these key features in explaining how ACAP1 achieves membrane binding and bending.

We also sought further confirmation of this overall conclusion. Based on the dimeric structure elucidated from crystallography, which predicts that the N terminus of one monomer extends closely to the C terminus of the other one (Figure 5J), we generated a fusion version of the ACAP1^{BAR-PH} dimer (BAR/PH-BAR/PH), using a sequence (GGGSGGRLGSSNSG) that is predicted to be able to extend across the ends of the two monomers to covalently link them (Figure 5J). The resulting fusion construct is predicted to retain the overall orientations of the monomers within the banana-like structure, with the BAR domains residing at the central portion and the PH domains residing at the distal portions. Gel filtration experiments suggested that the fusion protein folds and assembles correctly, as it has a similar profile with the nonfusion dimer (Figure S4G). As functional assessment, we found that the fusion dimer (BAR/PH-BAR/PH) retains the ability to tubulate liposomes (Figure 5K). We then generated a mutant version, a point mutation that targets only one PH domain (BAR/PH-BAR/PH [F280E]), and found that it could still induce liposome tubulation (Figure 5K). Notably, this result is in contrast to the effect of the F280E mutation in the conventional (nonfusion) version, which would have this point mutation in both PH domains, as we had found previously that it could no longer bind liposomes (see F280E in Figure 3B). Thus, this additional finding suggests that one PH domain is sufficient to confer the ability of the ACAP1^{BAR-PH} dimer to insert into membrane and impart curvature, which is in a good agreement with our cryo-EM observations.

(G and H) Structural model of ACAP1^{BAR-PH} helical assembly on the class II liposomal tubule. The color and labeling schemes are the same as that described in (C) and (D).

(I) Superposition between the ACAP1^{BAR-PH} tetramers of class I (red) and class II (blue).

(J) Structural basis for designing the fusion version of the ACAP1^{BAR-PH} dimer (BAR/PH-BAR/PH). The overall crystal structure of ACAP1^{BAR-PH} dimer is shown left and labeled with chain A and chain B for the two monomers. One distal region is zoomed in and shown (on right). The N terminus of chain B and the C terminus of chain A are labeled, respectively. The distance between the N terminus of chain B and the C terminus of chain A is ~37.8 Å. Thus, a linker (green) with the length of 14 amino acids (GGGSGGRLGSSNSG) is predicted to be sufficiently long to covalently link chain A and chain B via their termini.

(K) Negative-stain EM visualizing liposome tubulation; the scale bar represents 200 nm (see also Figures S4 and Movies S2, S3, S4, and S5).

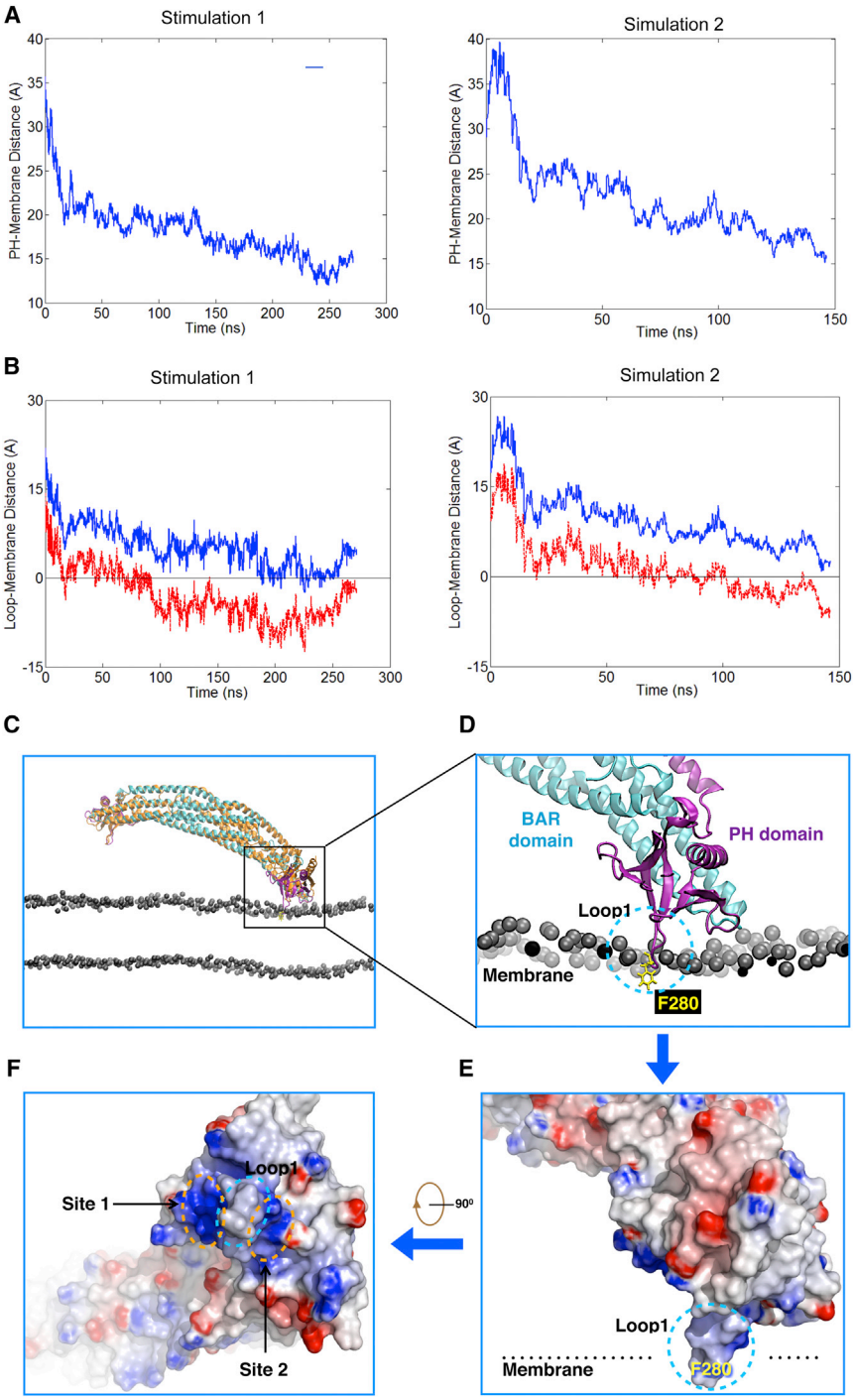

Figure 6. Molecular Simulation of ACAP1^{BAR-PH} Binding to Membrane

(A) The time evolution of the distance between the center of mass of one PH domain and the surface membrane phosphate plane.

(B) The time evolution of the distance between Loop1 in the PH domain and the surface membrane phosphate plane. The blue tracing tracks the distance between the center of mass of Loop1 and the membrane phosphate plane, while the red tracing tracks the distance between the F280 residue in Loop1 and the surface membrane phosphate plane. Negative values indicate an insertion of a particular protein structure into the membrane.

(C) Comparison of the crystal structure (shown in orange) and the final simulated model (shown in cyan and purple) of dimeric ACAP1^{BAR-PH} interacting with the membrane bilayer. Only the phosphate atoms of phospholipids in the membrane are shown for simplification.

(D) A zoomed-in view of (C), focusing on the PH domain engaging the membrane. The BAR and PH domains are shown as cartoon representation and colored in cyan and purple, respectively. The critical residue (F280) in Loop1 is shown embedded in membrane and represented in yellow. The phosphate atoms of the membrane phospholipids are shown as gray spheres.

(E) Electrostatic surface representation of the PH domain shown in the configuration illustrated in (D). Blue coloring highlights positive charges, while red coloring highlights negative charges.

(F) A 90° rotation of image shown in (E) to better visualize the membrane-binding surface of the PH domain. The positively charged patches (sites 1 and 2) and the hydrophobic insertion site (Loop1) are indicated (see also Figure S5 and Movies S6, S7, S8, and S9).

Molecular Simulation of ACAP1^{BAR-PH} Binding to Membrane

We next pursued molecular dynamics simulation to gain further insight into how these key features of the PH domain could be mediating interaction with the membrane. Two independent simulations (simulations 1 and 2) were performed with the time scale of 270 and 150 ns. Notably, both simulations revealed that the ACAP1^{BAR-PH} dimer behaves asymmetrically, with only one PH domain (chain A in simulation 1 and chain B in simulation 2) having a significant interaction with the membrane. This is reflected from the distance between the center mass of PH domain and the membrane phosphate plane, which decreased monotonically. In contrast, the other PH domain (chain B in simulation 1 and chain A in simulation 2) remained away from the membrane (Figure 6A; Movies S6 and S7). Loop1 in the PH domain was suggested to insert into the membrane at ~80 ns for simulation 1 and at ~100 ns for simulation 2. These insertions remained until the end of the simulation (Figures 6B and 6C; Movie S8).

Notably, the simulations revealed another mechanistic insight regarding how membrane insertion is achieved via the PH domain of ACAP1. In comparison to the crystal structure of ACAP1^{BAR-PH}, the membrane-bound ACAP1^{BAR-PH} from both simulations suggested a conformational rotation of the PH domain with respect to the BAR domain (Figure 6C and Movie S8), and then Loop1 adapts its orientation to facilitate the

insertion of F280 into membrane (Figures 6D and 6E). As such, the insertion of F280 into one leaf of the bilayer could reduce membrane surface tension asymmetrically and thereby induce membrane deformation when the dimeric ACAP1^{BAR-PH} becomes organized into higher ordered helical packing onto membrane.

Both simulations also suggested that there are two potential phosphoinositide binding sites (sites 1 and 2) along the sides of Loop1 (Figure 6F and Movie S8). These two sites are equivalent to the previous ones predicted from the crystal structure (Figures 2B and 2C) and comprise of residues K274/R286 for site 1 and residues R275/K281 for site 2. The importance of K274/R286 has already been suggested (see Figure 3A). We performed further mutation analysis on site 2 (R275/K281) by substituting with alanines (R275A/K281A) or by substituting lysines with aspartates and arginines with glutamates (R275E/K281D). These mutations revealed that alteration of site 2 also significantly eliminates the liposome binding of ACAP1^{BAR-PH} (Figure 3A).

We also noted that the observed asymmetric binding of ACAP1^{BAR-PH} dimer in both simulations further supports the cryo-EM model that predicts only one PH domain of one ACAP1^{BAR-PH} dimer inserts into the membrane (Figures 5D and 5H). This observation was not due to the mild asymmetric position of ACAP1^{BAR-PH} dimer at the start of the simulation because both PH domains of ACAP1^{BAR-PH} dimer were found capable of interacting with the membrane during the corresponding simulations (Movies S6 and S7). We then compared the final membrane bound ACAP1^{BAR-PH} with its starting conformation, i.e., the crystal structure. In both simulations, we found that besides the rotation of the PH domain for membrane insertion the BAR domains also exhibit significant distortion (Movie S9). The angle between the BAR domains and the membrane, which is defined as the angle between the 2-fold symmetric axis of the BAR domains and the membrane normal-plane that is across the BAR domains (Figure S5A), increased from 2.6 to 21 degrees in simulation 1 and decreased from 2.6 to −15 degrees in simulation 2 (Figure S5B). Thus, the repulsive distortion of the BAR domains could explain why the PH domains of the ACAP1^{BAR-PH} dimer interact asymmetrically with the membrane.

DISCUSSION

We have elucidated in molecular detail how ACAP1 achieves membrane remodeling for its role as a coat component that promotes the generation of transport carrier in endocytic recycling. Notably, this elucidation has uncovered unexpected features in both the BAR and PH domains in explaining their relative contributions to the ability of ACAP1 to bind and bend membrane.

Although the BAR domain in ACAP1 undergoes dimerization to form a banana-like structure, the electrostatic interaction between this curved protein structure and membrane is relatively weak. Thus, ACAP1 has an unconventional BAR domain, as it can achieve neither membrane binding nor bending by itself. Instead, we have identified key features in the neighboring PH domain, which are typically attributed to a conventional BAR domain in promoting membrane binding and curvature induction. The initial insight came from the crystal structural of ACAP1^{BAR-PH}. First, we identified a positively charged patch in the PH domain that could undergo electrostatic interaction with the negatively charged membrane surface to promote membrane binding. Second, we identified a loop that contains a bulky hydrophobic residue, which likely inserts into membrane to promote the generation of membrane curvature.

We then achieved significant insights by examining how the ACAP1^{BAR-PH} dimer is organized into a higher order structure on tubulated membrane. Pursuing cryo-EM studies, we find that the ACAP1^{BAR-PH} dimer shows lateral interactions with additional end-to-arch interactions. Notably, however, whereas the lateral interactions are mediated mainly by the BAR domains, the end-to-arch interactions are mediated mainly by the PH domains interacting with the BAR domains. Moreover, the ACAP1^{BAR-PH} dimer uses only one of its PH domains to contact the underlying membrane, while the other PH domain acts primary to interact with adjacent ACAP1^{BAR-PH} dimers. As such, rather than playing the primary role in membrane binding and curvature induction, the BAR domain in ACAP1 plays more of a supportive role in assisting the PH domain to bind and bend membrane.

Further insights into how the ACAP1^{BAR-PH} dimer initiates membrane binding for curvature induction have come from molecular simulation studies. Besides accounting for the key features elucidated for the PH domain, namely its positively charged patches and a key loop structure, in explaining how this domain acts in membrane binding and sculpting, the simulation studies revealed a further notable feature. Independently, both simulations suggested that only one PH domain of the ACAP1^{BAR-PH} dimer undergoes a rotational shift with respect to the BAR domain so that the positively charged patches in the PH domain can engage phosphoinositides of the membrane bilayer and thereby allow the key loop structure in this domain (Loop1) to be oriented properly for membrane insertion through a critical bulky hydrophobic residue (F280).

It is notable that, besides ACAP1, multiple other proteins are known to possess tandem BAR-PH domains. These include a number of ArfGAPs, as well as APPLs, and also sorting nexins that possess a PX domain that is highly similar to the PH domain (Cullen, 2008; Frost et al., 2009; Inoue and Randazzo, 2007; Pylypenko et al., 2007). As such, our insights regarding the PH domain in ACAP1 are likely relevant to a better understanding of how they act in membrane remodeling. On a broader note, the PH/PX domain is a prevalent structure, as it exists in many proteins (Lemmon, 2008; Rebecchi and Scarlata, 1998). Thus, our findings have the intriguing prospect of being relevant to a greater set of proteins than those currently known to participate in membrane remodeling.

EXPERIMENTAL PROCEDURES

Protein Crystallization

The ACAP1^{BAR-PH} protein was dialyzed against 20 mM Tris (pH 8.5) and concentrated to 3 mg/ml by ultrafiltration. The crystals were obtained using the hanging-drop vapor diffusion method at 16°C with the reservoir solution containing 0.2 M ammonium citrate (pH 7.0) and 10% PEG 3350. The addition of 6.0 mM Octyl beta-thioglucopyranoside yielded better single crystals that grew over a period of 3 days. The SeMet derivative was crystallized under the same condition as the native protein.

Data Collection and Structure Determination

The ACAP1^{BAR-PH} crystals were flash frozen in the reservoir solution with an additional 20% glycerol. The diffraction data of native crystals and single-wavelength (λ = 0.979 Å) anomalous diffraction data of SeMet derivatives were

collected at beamline BL5A and 17A (Photon Factory) and beamline BL17U (SSRF). All data were processed with the HKL2000 program suite (Table 1).

The crystal structure of ACAP1^{BAR-PH} was determined by a hybrid method combining single wavelength anomalous dispersion and molecular replacement. The initial selenium positions were determined using SHELXD (Usón and Sheldrick, 1999). The selenium atoms were refined, and initial phases were generated using SOLVE (Terwilliger and Berendzen, 1999). Phase improvement and density modification were performed using the program RESOLVE (Terwilliger, 2000). Initial model was built automatically using the Quick-Fold of ARP/WARP (Langer et al., 2008). Almost all BAR domain backbones were automatically traced, while the PH domain exhibited only several noncontinuous fragments. Molecular replacement of two PH domains was then performed using MOLREP (Vagin and Teplyakov, 2010) based on the single-wavelength anomalous diffraction experimental density map. An iterative method (Yao et al., 2006; Zhang et al., 2010) combining OASIS (Fan and Gu, 1985), DM (Bailey, 1994) and REOLVE (Terwilliger, 2000) was then used to further improve the phases and thereby complete model building. Model building was further improved manually using COOT (Emsley and Cowtan, 2004). Structure refinement was done using Refmac5 (Murshudov et al., 1997) and CNS (Brünger et al., 1998). The statistics of the data processing and structure refinement are summarized in Table 1. All of the figures for structural illustration were generated with Pymol (http://www.pymol.org) or UCSF Chimera (Pettersen et al., 2004).

Cryo-EM and Helical Reconstruction

The ACAP1^{BAR-PH} protein (4 mg/ml) was incubated with 200 nm diameter liposomes (2 mg/ml) at room temperature for 60 minutes. A drop (3.5 μl) of the mixture was then applied onto a 300-mesh GiG holy carbon grid (Jiangsu Life-Trust) that was pretreated in plasma cleaner (PDC-32G, HARRICK PLASMA). The grid was then blotted for 3.0 s with a blot force 2 at 100% humidity, using FEI Vitrobot (Mark IV) before it was quickly frozen in liquid ethane that was cooled by liquid nitrogen.

The ACAP1^{BAR-PH} coating membrane tubules were imaged with a FEI Titan Krios cryo-EM that was operated under 300 kV and equipped with a Gatan UltraScan4000 charge-coupled device camera. Low-dose images (20 e^{-}/Å^2) were collected manually. The nominal magnification was set to 75,000×, which corresponds to a pixel size 1.196 Å. The defocus range was set to 2.5∼3.5 μm. A total of 259 cryo-EM micrographs were collected.

The defocus value of each micrograph was determined by CTFFIND3 (Mindell and Grigorieff, 2003). About 160 ACAP1^{BAR-PH} tubules were selected using the helical option "helixboxer" in EMAN1 (Ludtke et al., 1999). All of the selected tubules were padded to 4,096 × 4,096 pixels to obtain diffraction pattern in Fourier space. These tubules were then classified into two main classes (class I and class II) according to their different diffraction pattern. For each of class, further reference-free classification was performed using e2refine2d.py in EMAN2 (Tang et al., 2007). All of the class averages were rotated to normalize the orientation of all of the tubules in the vertical direction. The diameters of each class of ACAP1^{BAR-PH} tubules were calculated by projecting the images in the horizontal direction to further sort the tubules; 304 segments were selected from 10 tubules with 95.5% overlap for class I, whereas 352 segments were selected from six tubules with 88.3% overlap for class II.

Initial helical parameters (Δφ and ΔZ), which denote the rise and the rotation angle between the two neighboring subunits, respectively, were estimated by calculating the order of Fourier-Bessel function from the layer lines of diffraction patterns (see Figure 4F). For class I, the initial parameters (Δφ and ΔZ) are 42.7° and 23.2 Å, respectively, which yielded two starting numbers ($n_1 = -15$ and $n_2 = 9$), implying the existence of a C3 symmetry in this class. For class II, the initial parameters (Δφ and ΔZ) are 65.9° and 6.7 Å, respectively, which yielded two starting numbers ($n_1 = -16$ and $n_2 = 11$). These initial parameters were input into the IHRSR program (Egelman, 2000) by using a cylinder as a starting model. All of the images of raw particles were binned three times before subjecting into the refinement by IHRSR. The out-of-plane tilt angles were considered during the refinement for both classes. The helical parameters finally converged to Δφ = 42.72°and ΔZ = 23.20 Å for class I and to Δφ = 65.90°and ΔZ = 6.67 Å for class II. Nearly 82% of class I filaments show a significant out-of-plane tilt angle, and ∼54% of class II filaments show the significant out-of-plane tilt angles (see Figures S4E and S4F), which increases the difficulty of helical reconstructions.

The nominal resolutions of the reconstructed volumes were assessed by computing the FSC between the cryo-EM map and the fitted structural models and by using the threshold cutoffs 0.5 and 0.143. The handedness of the cryo-EM map was determined by judging the fit of the structural model of ACAP1-$^{BAR-PH}$ dimer into the map. Cryo-EM maps were segmented, displayed, and fitted with atomic models using UCSF Chimera (Pettersen et al., 2004). All structural figures were generated by UCSF Chimera (Pettersen et al., 2004).

Molecular Dynamics Simulation

The molecular dynamics simulations were performed using NAMD 2.9 (Phillips et al., 2005) and the CHARM 22/27 force field with CMAP correction (Mackerell et al., 2004). Simulations were performed under constant NPT (a fixed number of atoms N, pressure P, and temperature T) conditions and periodic boundary conditions. The temperature was maintained throughout at 310 K using a Langevin thermostat with a 5 ps^{-1} damping coefficient. The system pressure was maintained at 1 atm using a Langevin piston barostat. Electrostatic interactions were calculated using the particle mesh Ewald sum method (Darden et al., 1993) with a cutoff of 12 Å. An integration time step of 2 fs was used while constraining all hydrogen-containing covalent bonds with the SHAKE algorithm (Ryckaert et al., 1977).

The CHARMM-GUI (Jo et al., 2008) was employed to generate a lipid bilayer of 40% DOPC/30%DOPE/20%POPS/10% DAPC. DAPC was then replaced by PI(4,5)P_2. The crystal structure of ACAP1^{BAR-PH} was placed to the top of the membrane. The closest point of the protein was 9.5 Å from the membrane surface phosphate plane. The system was solvated with TIP3P water and neutralized by K+ and Cl− counter ions. The membrane-protein system was equilibrated using a stepwise relaxation procedure. After all restraints on C alpha of the protein atoms were removed, two independent regular NPT simulations were executed. A total of 270 and 150 ns of data were generated for simulation 1 and simulation 2, respectively.

Other methods are detailed in the Supplemental Information.

ACCESSION NUMBERS

The coordinate of ACAP1^{BAR-PH} crystal structure has been deposited in the Protein Data Bank (PDB) with the accession code 4NSW. The EM maps of helical tubules have been deposited in Electron Microscopy Data Bank (EMDB) with the accession codes EMD-2546 for class I and EMD-2547 for class II, respectively. The corresponding fitted coordinates of ACAP1^{BAR-PH} helical array on the tubule have been deposited in the PDB with the accession codes 4CKG and 4CKH, respectively.

SUPPLEMENTAL INFORMATION

Supplemental Information includes Supplemental Experimental Procedures, five figures, and nine movies and can be found with this article online at http://dx.doi.org/10.1016/j.devcel.2014.08.020.

AUTHOR CONTRIBUTIONS

F.S. and V.H. initiated and supervised the project. X.P., V.H., and F.S. designed all experiments. X.P., K.Z., J.M., and Q.Z. performed crystallographic work. X.P., Y.Z., B.G., E.H.E., and Y.D. performed EM work. X.P. and B.G. performed mutagenesis studies. J.F. performed molecular dynamics simulations. J.L. performed vesicle reconstitution studies. X.P., J.F., Y.Z., J.L., V.H., and F.S. analyzed the data. X.P., J.F., and Y.Z. contributed to manuscript preparation. V.H. and F.S. wrote the manuscript.

ACKNOWLEDGMENTS

This work was supported with grants to F.S. by the Chinese Ministry of Science and Technology (2011CB910301 and 2011CB910901), grants to X.P and Y.Z. by the National Natural Science Foundation of China (31000635 and 31100617), grants to J.F. by the City University of Hong Kong (Projects no. 7200350 and 9610291), grants to V.H. by the NIH (GM073016 and GM058615), and a grant to E.H.E. by the NIH (EB001567). All of the EM data were collected and most molecular dynamics simulations were performed at

Center for Biological Imaging (CBI, http://cbi.ibp.ac.cn), Institute of Biophysics, Chinese Academy of Sciences. We are grateful to Dr. Gang Ji (CBI) for his assistance in EM data collection.

Received: June 10, 2014
Revised: August 12, 2014
Accepted: August 21, 2014
Published: October 2, 2014

REFERENCES

Bai, J., Hu, Z., Dittman, J.S., Pym, E.C., and Kaplan, J.M. (2010). Endophilin functions as a membrane-bending molecule and is delivered to endocytic zones by exocytosis. Cell *143*, 430–441.

Bai, M., Pang, X., Lou, J., Zhou, Q., Zhang, K., Ma, J., Li, J., Sun, F., and Hsu, V.W. (2012). Mechanistic insights into regulated cargo binding by ACAP1 protein. J. Biol. Chem. *287*, 28675–28685.

Bailey, S.; Collaborative Computational Project, Number 4 (1994). The CCP4 suite: programs for protein crystallography. Acta Crystallogr. D Biol. Crystallogr. *50*, 760–763.

Boucrot, E., Pick, A., Çamdere, G., Liska, N., Evergren, E., McMahon, H.T., and Kozlov, M.M. (2012). Membrane fission is promoted by insertion of amphipathic helices and is restricted by crescent BAR domains. Cell *149*, 124–136.

Brünger, A.T., Adams, P.D., Clore, G.M., DeLano, W.L., Gros, P., Grosse-Kunstleve, R.W., Jiang, J.S., Kuszewski, J., Nilges, M., Pannu, N.S., et al. (1998). Crystallography & NMR system: a new software suite for macromolecular structure determination. Acta Crystallogr. D Biol. Crystallogr. *54*, 905–921.

Ceccarelli, D.F., Blasutig, I.M., Goudreault, M., Li, Z., Ruston, J., Pawson, T., and Sicheri, F. (2007). Non-canonical interaction of phosphoinositides with pleckstrin homology domains of Tiam1 and ArhGAP9. J. Biol. Chem. *282*, 13864–13874.

Cronin, T.C., DiNitto, J.P., Czech, M.P., and Lambright, D.G. (2004). Structural determinants of phosphoinositide selectivity in splice variants of Grp1 family PH domains. EMBO J. *23*, 3711–3720.

Cullen, P.J. (2008). Endosomal sorting and signalling: an emerging role for sorting nexins. Nat. Rev. Mol. Cell Biol. *9*, 574–582.

Dai, J., Li, J., Bos, E., Porcionatto, M., Premont, R.T., Bourgoin, S., Peters, P.J., and Hsu, V.W. (2004). ACAP1 promotes endocytic recycling by recognizing recycling sorting signals. Dev. Cell *7*, 771–776.

Darden, T., York, D., and Pedersen, L. (1993). Particle mesh Ewald: an N•Log(N) method for Ewald sums in large systems. J. Chem. Phys. *98*, 10089–10092.

Egelman, E.H. (2000). A robust algorithm for the reconstruction of helical filaments using single-particle methods. Ultramicroscopy *85*, 225–234.

Emsley, P., and Cowtan, K. (2004). Coot: model-building tools for molecular graphics. Acta Crystallogr. D Biol. Crystallogr. *60*, 2126–2132.

Fan, H.F., and Gu, Y.X. (1985). Combining direct methods with isomorphous replacement or anomalous scattering data. III. The incorporation of partial structure information. Acta Crystallogr. *A41*, 280–284.

Ferguson, K.M., Kavran, J.M., Sankaran, V.G., Fournier, E., Isakoff, S.J., Skolnik, E.Y., and Lemmon, M.A. (2000). Structural basis for discrimination of 3-phosphoinositides by pleckstrin homology domains. Mol. Cell *6*, 373–384.

Frost, A., Perera, R., Roux, A., Spasov, K., Destaing, O., Egelman, E.H., De Camilli, P., and Unger, V.M. (2008). Structural basis of membrane invagination by F-BAR domains. Cell *132*, 807–817.

Frost, A., Unger, V.M., and De Camilli, P. (2009). The BAR domain superfamily: membrane-molding macromolecules. Cell *137*, 191–196.

Gallop, J.L., Jao, C.C., Kent, H.M., Butler, P.J., Evans, P.R., Langen, R., and McMahon, H.T. (2006). Mechanism of endophilin N-BAR domain-mediated membrane curvature. EMBO J. *25*, 2898–2910.

Inoue, H., and Randazzo, P.A. (2007). Arf GAPs and their interacting proteins. Traffic *8*, 1465–1475.

Itoh, T., and De Camilli, P. (2006). BAR, F-BAR (EFC) and ENTH/ANTH domains in the regulation of membrane-cytosol interfaces and membrane curvature. Biochim. Biophys. Acta *1761*, 897–912.

Jackson, T.R., Brown, F.D., Nie, Z., Miura, K., Foroni, L., Sun, J., Hsu, V.W., Donaldson, J.G., and Randazzo, P.A. (2000). ACAPs are arf6 GTPase-activating proteins that function in the cell periphery. J. Cell Biol. *151*, 627–638.

Jo, S., Kim, T., Iyer, V.G., and Im, W. (2008). CHARMM-GUI: a web-based graphical user interface for CHARMM. J. Comput. Chem. *29*, 1859–1865.

King, G.J., Stöckli, J., Hu, S.H., Winnen, B., Duprez, W.G., Meoli, C.C., Junutula, J.R., Jarrott, R.J., James, D.E., Whitten, A.E., and Martin, J.L. (2012). Membrane curvature protein exhibits interdomain flexibility and binds a small GTPase. J. Biol. Chem. *287*, 40996–41006.

Langer, G., Cohen, S.X., Lamzin, V.S., and Perrakis, A. (2008). Automated macromolecular model building for X-ray crystallography using ARP/wARP version 7. Nat. Protoc. *3*, 1171–1179.

Lemmon, M.A. (2008). Membrane recognition by phospholipid-binding domains. Nat. Rev. Mol. Cell Biol. *9*, 99–111.

Li, J., Mao, X., Dong, L.Q., Liu, F., and Tong, L. (2007a). Crystal structures of the BAR-PH and PTB domains of human APPL1. Structure *15*, 525–533.

Li, J., Peters, P.J., Bai, M., Dai, J., Bos, E., Kirchhausen, T., Kandror, K.V., and Hsu, V.W. (2007b). An ACAP1-containing clathrin coat complex for endocytic recycling. J. Cell Biol. *178*, 453–464.

Li, J., Malaby, A.W., Famulok, M., Sabe, H., Lambright, D.G., and Hsu, V.W. (2012). Grp1 plays a key role in linking insulin signaling to glut4 recycling. Dev. Cell *22*, 1286–1298.

Ludtke, S.J., Baldwin, P.R., and Chiu, W. (1999). EMAN: semiautomated software for high-resolution single-particle reconstructions. J. Struct. Biol. *128*, 82–97.

Lumb, C.N., He, J., Xue, Y., Stansfeld, P.J., Stahelin, R.V., Kutateladze, T.G., and Sansom, M.S. (2011). Biophysical and computational studies of membrane penetration by the GRP1 pleckstrin homology domain. Structure *19*, 1338–1346.

Mackerell, A.D., Jr., Feig, M., and Brooks, C.L., 3rd. (2004). Extending the treatment of backbone energetics in protein force fields: limitations of gas-phase quantum mechanics in reproducing protein conformational distributions in molecular dynamics simulations. J. Comput. Chem. *25*, 1400–1415.

Mim, C., and Unger, V.M. (2012). Membrane curvature and its generation by BAR proteins. Trends Biochem. Sci. *37*, 526–533.

Mim, C., Cui, H., Gawronski-Salerno, J.A., Frost, A., Lyman, E., Voth, G.A., and Unger, V.M. (2012). Structural basis of membrane bending by the N-BAR protein endophilin. Cell *149*, 137–145.

Mindell, J.A., and Grigorieff, N. (2003). Accurate determination of local defocus and specimen tilt in electron microscopy. J. Struct. Biol. *142*, 334–347.

Mizuno, N., Jao, C.C., Langen, R., and Steven, A.C. (2010). Multiple modes of endophilin-mediated conversion of lipid vesicles into coated tubes: implications for synaptic endocytosis. J. Biol. Chem. *285*, 23351–23358.

Murshudov, G.N., Vagin, A.A., and Dodson, E.J. (1997). Refinement of macromolecular structures by the maximum-likelihood method. Acta Crystallogr. D Biol. Crystallogr. *53*, 240–255.

Peter, B.J., Kent, H.M., Mills, I.G., Vallis, Y., Butler, P.J.G., Evans, P.R., and McMahon, H.T. (2004). BAR domains as sensors of membrane curvature: the amphiphysin BAR structure. Science *303*, 495–499.

Pettersen, E.F., Goddard, T.D., Huang, C.C., Couch, G.S., Greenblatt, D.M., Meng, E.C., and Ferrin, T.E. (2004). UCSF Chimera—a visualization system for exploratory research and analysis. J. Comput. Chem. *25*, 1605–1612.

Phillips, J.C., Braun, R., Wang, W., Gumbart, J., Tajkhorshid, E., Villa, E., Chipot, C., Skeel, R.D., Kalé, L., and Schulten, K. (2005). Scalable molecular dynamics with NAMD. J. Comput. Chem. *26*, 1781–1802.

Pykäläinen, A., Boczkowska, M., Zhao, H., Saarikangas, J., Rebowski, G., Jansen, M., Hakanen, J., Koskela, E.V., Peränen, J., Vihinen, H., et al. (2011). Pinkbar is an epithelial-specific BAR domain protein that generates planar membrane structures. Nat. Struct. Mol. Biol. *18*, 902–907.

Pylypenko, O., Lundmark, R., Rasmuson, E., Carlsson, S.R., and Rak, A. (2007). The PX-BAR membrane-remodeling unit of sorting nexin 9. EMBO J. *26*, 4788–4800.

Rebecchi, M.J., and Scarlata, S. (1998). Pleckstrin homology domains: a common fold with diverse functions. Annu. Rev. Biophys. Biomol. Struct. *27*, 503–528.

Ross, J.A., Chen, Y., Müller, J., Barylko, B., Wang, L., Banks, H.B., Albanesi, J.P., and Jameson, D.M. (2011). Dimeric endophilin A2 stimulates assembly and GTPase activity of dynamin 2. Biophys. J. *100*, 729–737.

Ryckaert, J.P., Ciccotti, G., and Berendsen, H.J.C. (1977). Numerical integration of cartesian equations of motion of a system with constraints: molecular dynamics of n-alkanes. J. Comp. Physiol. *23*, 327–341.

Shimada, A., Niwa, H., Tsujita, K., Suetsugu, S., Nitta, K., Hanawa-Suetsugu, K., Akasaka, R., Nishino, Y., Toyama, M., Chen, L., et al. (2007). Curved EFC/F-BAR-domain dimers are joined end to end into a filament for membrane invagination in endocytosis. Cell *129*, 761–772.

Shinozaki-Narikawa, N., Kodama, T., and Shibasaki, Y. (2006). Cooperation of phosphoinositides and BAR domain proteins in endosomal tubulation. Traffic *7*, 1539–1550.

Tang, G., Peng, L., Baldwin, P.R., Mann, D.S., Jiang, W., Rees, I., and Ludtke, S.J. (2007). EMAN2: an extensible image processing suite for electron microscopy. J. Struct. Biol. *157*, 38–46.

Terwilliger, T.C. (2000). Maximum-likelihood density modification. Acta Crystallogr. D Biol. Crystallogr. *56*, 965–972.

Terwilliger, T.C., and Berendzen, J. (1999). Automated MAD and MIR structure solution. Acta Crystallogr. D Biol. Crystallogr. *55*, 849–861.

Usón, I., and Sheldrick, G.M. (1999). Advances in direct methods for protein crystallography. Curr. Opin. Struct. Biol. *9*, 643–648.

Vagin, A., and Teplyakov, A. (2010). Molecular replacement with MOLREP. Acta Crystallogr. D Biol. Crystallogr. *66*, 22–25.

Yao, D.Q., Huang, S., Wang, J.W., Gu, Y.X., Zheng, C.D., Fan, H.F., Watanabe, N., and Tanaka, I. (2006). SAD phasing by OASIS-2004: case studies of dual-space fragment extension. Acta Crystallogr. D Biol. Crystallogr. *62*, 883–890.

Yu, H., and Schulten, K. (2013). Membrane sculpting by F-BAR domains studied by molecular dynamics simulations. PLoS Comput. Biol. *9*, e1002892.

Zhang, T., Wu, L.J., Gu, Y.X., Zheng, C.D., and Fan, H.F. (2010). Combining SAD/SIR iteration and MR iteration in partial-model extension of proteins. Chinese Phys. B *19*, 096101.

Zhu, G., Chen, J., Liu, J., Brunzelle, J.S., Huang, B., Wakeham, N., Terzyan, S., Li, X., Rao, Z., Li, G., and Zhang, X.C. (2007). Structure of the APPL1 BAR-PH domain and characterization of its interaction with Rab5. EMBO J. *26*, 3484–3493.